Electronic Supplementing Information (ESI)

Impact of static and dynamic disorder effects on the charge transport properties of merocyanine single crystals

Nora Gildemeister[a#], Sven Geller[a#], Robert Herzhoff[a], Fabrizia Negri[b], Klaus Meerholz*[a], Daniele Fazzi*[a,b]

[a]Institut für Physikalische Chemie, Department für Chemie, Universität zu Köln, Greinstr. 4-6, 50939, Köln, Germany

[b]Università di Bologna, Dipartimento di Chimica 'Giacomo Ciamician', Via P. Gobetti, 85, 40129, Bologna, Italy.

# These authors contributed equally to the work.

Corresponding authors: *klaus.meerholz@uni-koeln.de, daniele.fazzi@unibo.it*

Table of Contents

1. Bond Length Alternation Patterns and Reorganization Energy

For BLA patterns of *pyrl,tbu*-**D1A1**, *nbu,tbu*- and *hex,tbu*-**D2A1** see Ref. 1.

a) *nbu,nbu*-**DA** b) *oct,tbu*-**DA**

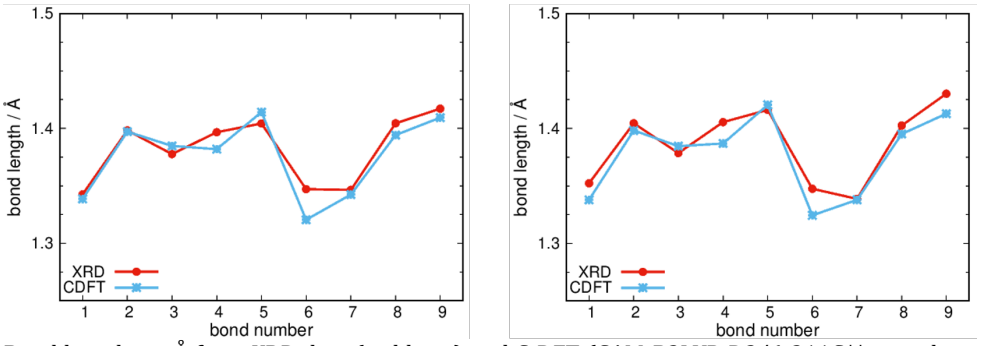

Figure S1: Bond lengths in Å from XRD data (red lines) and C-DFT (CAM-B3LYP-D3/6-311G**, gas phase, blue lines, $\boldsymbol{\delta^{D/A} = \pm 0.6q}$) for a) *nbu,nbu*- and b) *oct,tbu*-**D2A1**.

Table S1: $\mathbf{d_{BLA}}$ (Å) values as derived from XRD data and calculated via C-DFT (CAM-B3LYP-D3/6-311G**, $\boldsymbol{\delta^{D/A} = \pm 0.6q}$) for the neutral ground state (GS) and with C-DFT (CAM-B3LYP-D3/6-311G**, $\boldsymbol{\delta^{D/A} = \pm 0.0q}$) for the charged ground state (GS).

R1,R2-**D2A1**	$\boldsymbol{d_{BLA}}$ **(XRD)** Å	$\boldsymbol{d_{BLA}}$ **(C-DFT) Neutral GS** Å	$\boldsymbol{d_{BLA}}$ **Charged GS** Å
me,tbu-	-0.003	0.009	-0.018
bpr,tbu -	-0.002	0.009	-0.019
nbu,tbu -	0.001[1]	0.002[1]	-0.027[1]
nbu,nbu-	-0.003	0.010	-0.013
hex,tbu -	-0.002[1]	0.003[1]	-0.027[1]
oct,tbu -	0.000	0.008	-0.020
pyrl,tbu-**D1A1**	-0.009[1]	-0.010[1]	-0.018[1]

Table S2: Internal hole reorganization energies ($\boldsymbol{\lambda_i^{AP/HR}}$, **meV**) as computed at the C-DFT (CAM-B3LYP-D3/6-311G**, $\boldsymbol{\delta^{D/A} = \pm 0.6q}$) level.

R1,R2-**D2A1**	$\boldsymbol{\lambda_i^{AP}}$
me,tbu-	167
bpr,tbu -	179
nbu,tbu -	178[1]
nbu,nbu-	167
hex,tbu -	177[1]
oct,tbu -	175
pyrl,tbu-**D1A1**	127[1]

2. Crystal Supercell Analysis

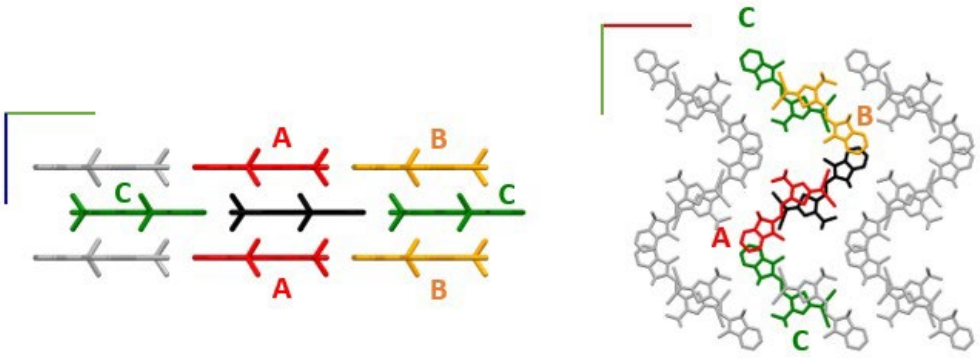

Figure S2: Different views of a supercell of the crystal structure of *me,tbu*-**D2A1**. The central molecule (black) and nearest neighbours considered in the kinetic Monte Carlo simulations.

Table S3: Computed (ωB97X-D3/6-311G**) charge transfer integrals (J_{ij}) and Brownian transfer rates (k_{ET}) as calculated with the Marcus theory for each dimer belonging to *me,tbu*-**D2A1**.

Dimer	J/meV	k_{ET}/s^{-1}
A	59	1.5 x 10^{13}
B	14	8.9 x 10^{11}
C	4	7.4 x 10^{10}

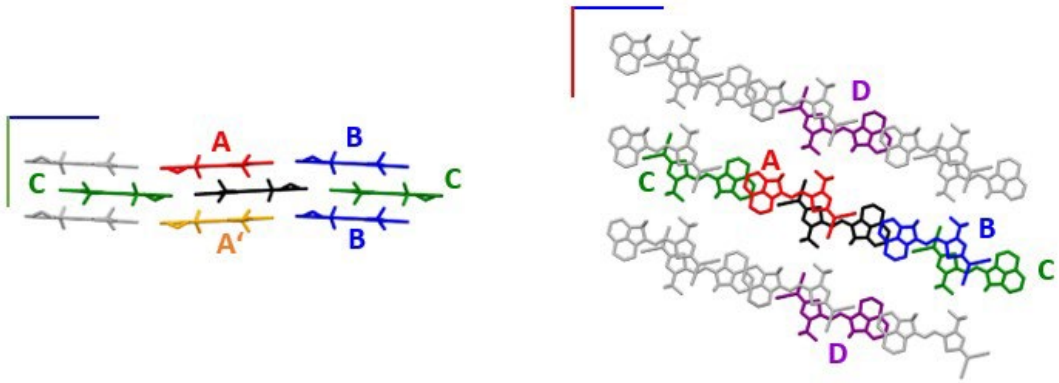

Figure S3: Different views of a supercell of the crystal structure of *bpr,tbu*-**D2A1**. The central molecule (black) and nearest neighbours considered in the kinetic Monte Carlo simulations.

Table S4: Computed (ωB97X-D3/6-311G**) charge transfer integrals (J_{ij}) and Brownian transfer rates (k_{ET}) as calculated with the Marcus theory for each dimer belonging to *bpr,tbu*-**D2A1**.

Dimer	J_{ij}/meV	k_{ET}/s^{-1}
A	34	4.4 x 10^{13}
A’	8	2.4 x 10^{11}
B	16	1.0 x 10^{12}
C	3	4.5 x 10^{10}
D	1	3.7 x 10^{9}

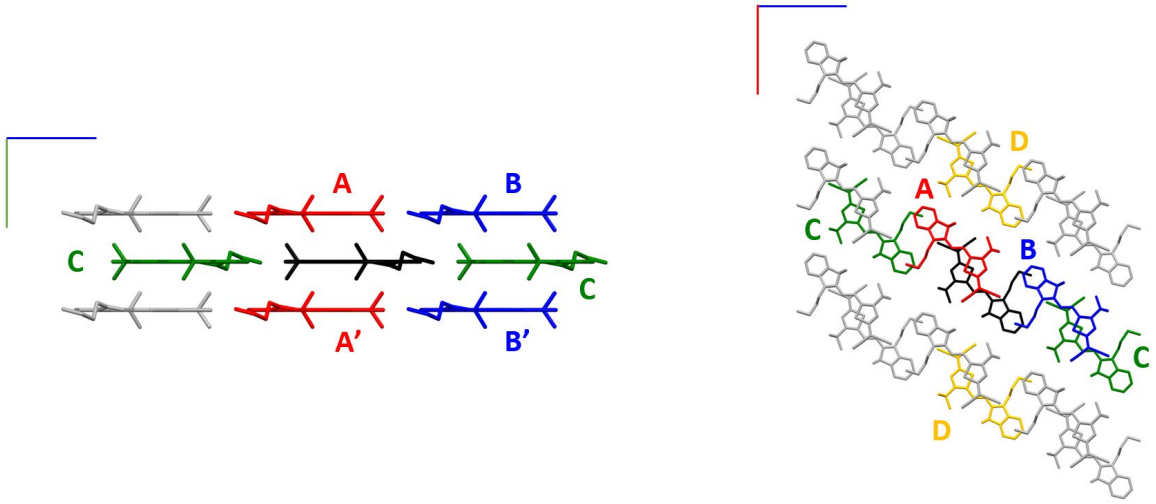

Figure S4: Different views of a supercell of the crystal structure of *nbu,tbu*-**D2A1**. The central molecule (black) and nearest neighbours considered in the kinetic Monte Carlo simulations.

Table S5: Computed (ωB97X-D3/6-311G**) charge transfer integrals (J_{ij}) and Brownian transfer rates (k_{ET}) as calculated with the Marcus theory for each dimer belonging to *nbu,tbu*-**D2A1**.

Dimer	J_{ij}/meV	k_{ET}/s^{-1}
A	16	1.0 x 10^{12}
A'	11	4.9 x 10^{11}
B	2	2.1 x 10^{10}
B'	4	5.0 x 10^{10}
C	3	3.6 x 10^{10}
D	4	7.3 x 10^{10}

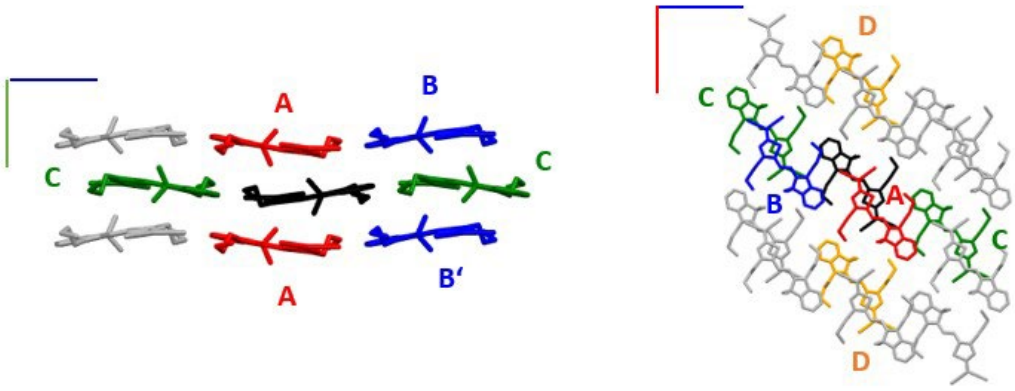

Figure S5: Different views of a supercell of the crystal structure of *nbu,nbu*-**D2A1**. The central molecule (black) and nearest neighbours considered in the kinetic Monte Carlo simulations.

Table S6: Computed (ωB97X-D3/6-311G**) charge transfer integrals (J_{ij}) and Brownian transfer rates (k_{ET}) as calculated with the Marcus theory for each dimer belonging to *nbu,nbu*-**D2A1**.

Dimer	J_{ij}/meV	k_{ET}/s^{-1}
A	6	1.5 x 10^{11}
B	8	2.7 x 10^{11}
B'	6	1.3 x 10^{11}
C	6	1.3 x 10^{11}
D	3	3.5 x 10^{10}

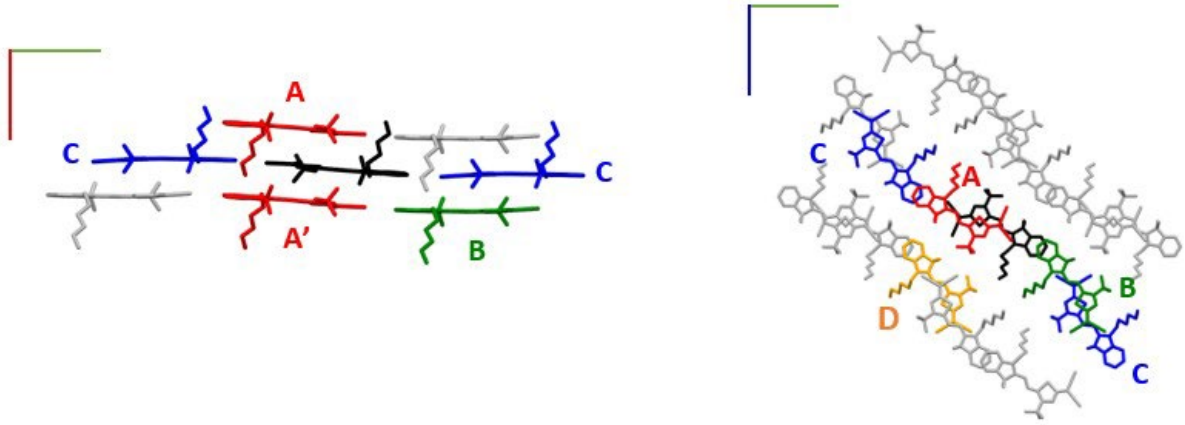

Figure S6: Different views of a supercell of the crystal structure of *hex,tbu*-**D2A1**. The central molecule (black) and nearest neighbours considered in the kinetic Monte Carlo simulations.

Table S7: Computed (ωB97X-D3/6-311G**) charge transfer integrals (J_{ij}) and Brownian transfer rates (k_{ET}) as calculated with the Marcus theory for each dimer belonging to *hex,tbu*-**D2A1**.

Dimer	J_{ij}/meV	k_{ET}/s^{-1}
A	46	1.5 x 10^{13}
A'	64	2.9 x 10^{13}
B	3	2.6 x 10^{10}
C	2	9.3 x 10^{9}
D	4	9.3 x 10^{10}

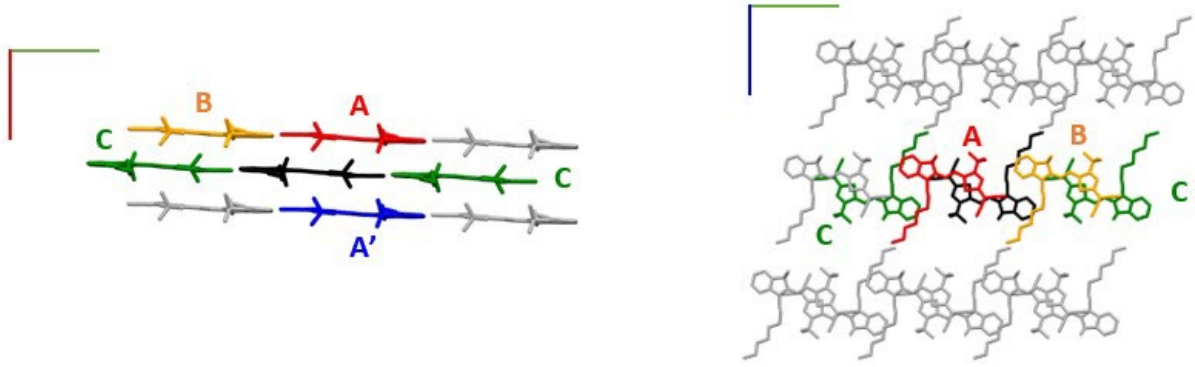

Figure S7: Different views of a supercell of the crystal structure of *oct,tbu*-**D2A1**. The central molecule (black) and nearest neighbours considered in the kinetic Monte Carlo simulations.

Table S8: Computed (ωB97X-D3/6-311G**) charge transfer integrals (J_{ij}) and Brownian transfer rates (k_{ET}) as calculated with the Marcus theory for each dimer belonging to *oct,tbu*-**D2A1**.

Dimer	J_{ij}/meV	k_{ET}/s^{-1}
A	80	2.6 x 10^{13}
A'	31	3.8 x 10^{12}
B	4	5.7 x 10^{10}
C	3	3.5 x 10^{10}

3. Supercell of *pyrl,tbu*-D1A1

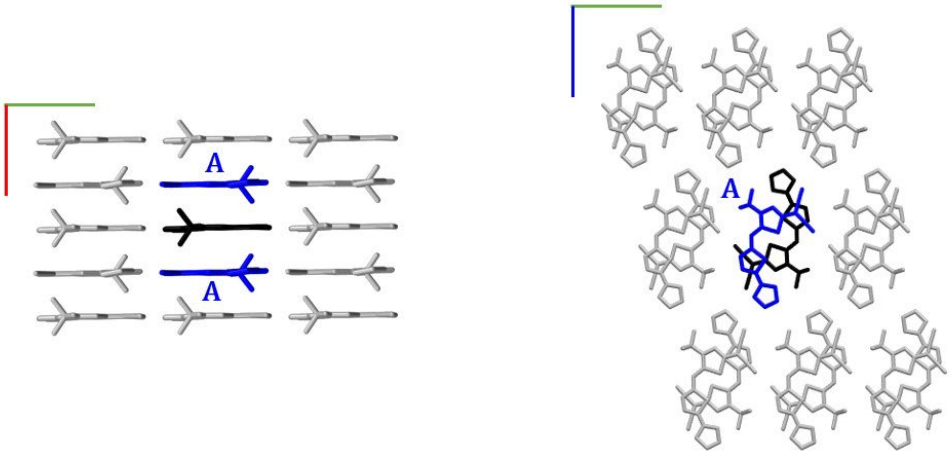

Figure S8: Different views of a supercell of the crystal structure of *pyrl,tbu*-**D1A1**. The central molecule (black) and nearest neighbour with transfer integral of 56 meV in blue and transfer integrals below or equal to 4 meV in grey.

4. Network Analysis

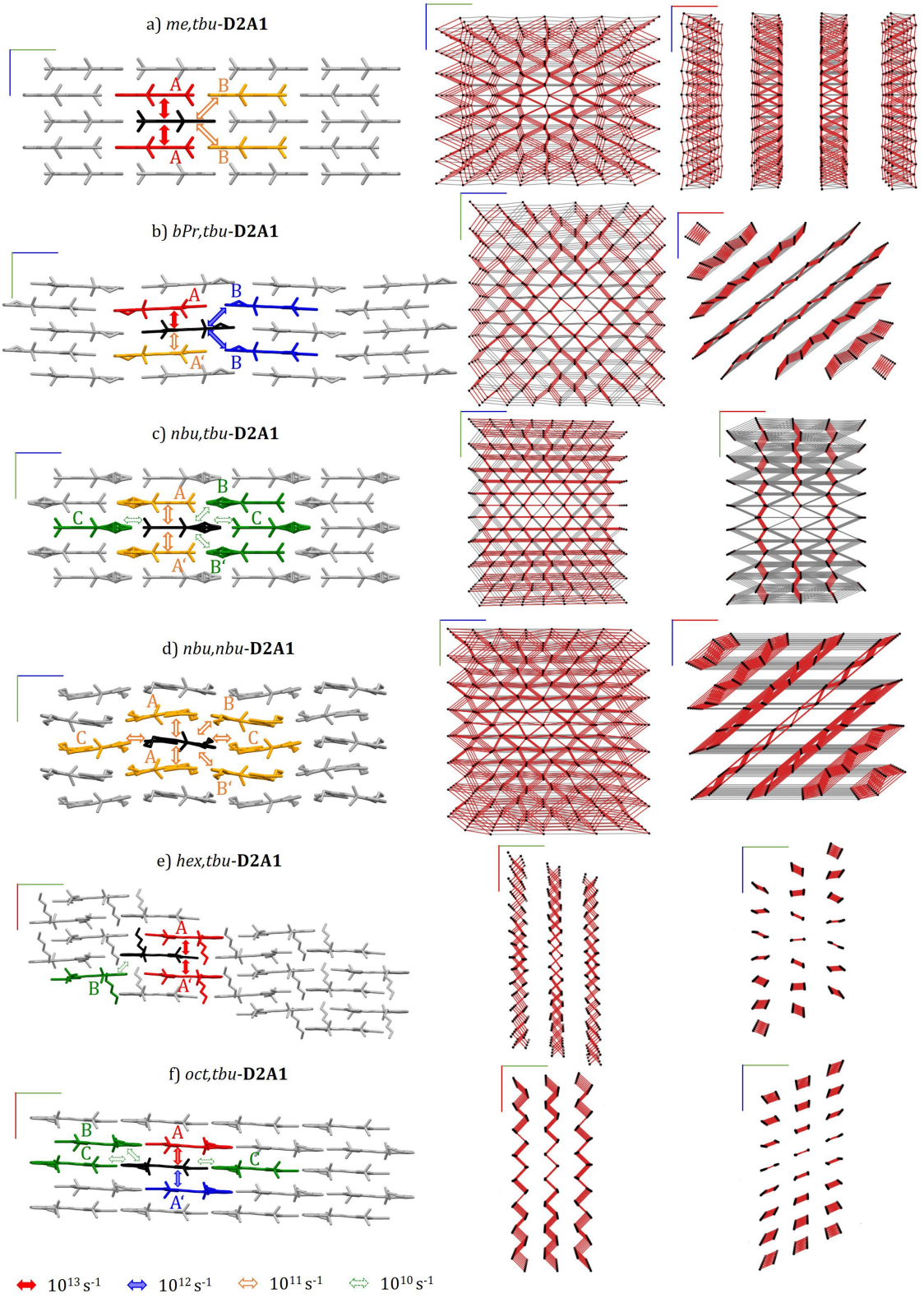

Figure S9: Left: Side view onto the long axis of the crystal structures. For each crystal is reported a schematic view of the charge transport pathways from the central molecule (black) to the nearest neighbour molecules (red, blue, orange, green) showing $J_{ij} \geq 3$ meV and $k_{ET} \geq 10^{10}$ s^{-1}. Middle and Right: Topology of charge transport network. Nodes correspond to molecular centers of mass (black dots) and edges according to the absolute values of transfer integrals for highest couplings (red) and moderate couplings (grey). Axes correspond to Cartesian axes x (red), y (green) and z (blue).

5. Crystallographic Data of *oct,tbu*-D2A1

Table S9: Crystallographic Parameters of *oct,tbu*-**D2A1.**

a (Å)	7.3149
b (Å)	14.8933
c (Å)	15.519
α (°)	105.826
β (°)	90.588
γ (°)	91.263

6. Site Energy Difference Distributions

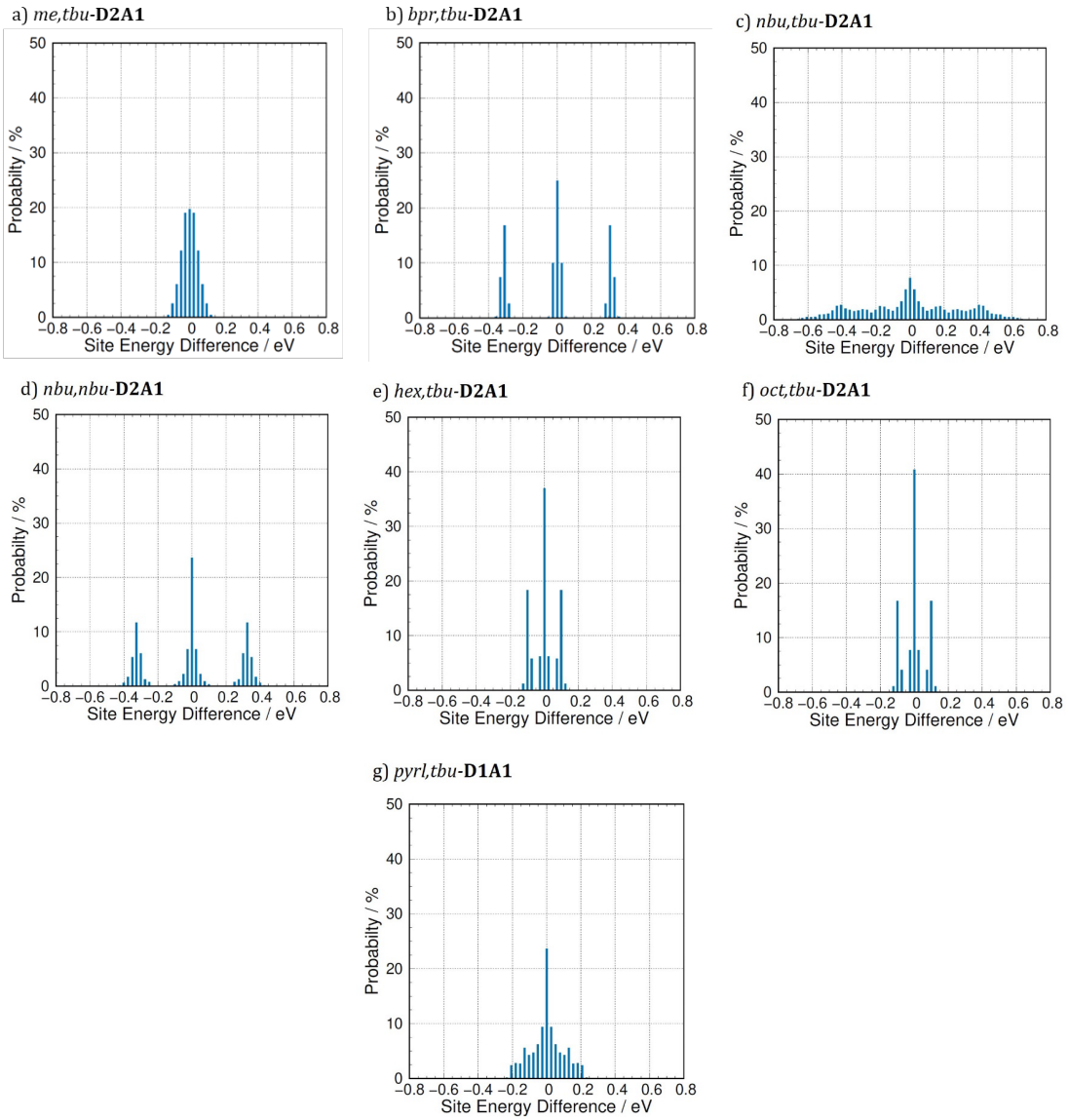

Figure S10: Site energy difference distributions ΔE_{ij} of a) *me,tbu*-, b) *bpr,tbu*-, c) *nbu,tbu*-, d) *nbu,nbu*-, e) *hex,tbu*- and f) *oct,tbu*-**D2A1** and g) *pyrl,tbu*-**D1A1**.

7. Impact of Static Disorder onto Rate Constants

Table S10: Computed transfer rates k_{eT} (s^{-1}) for intra- and inter-columnar dimers (long axis), when static disorder is included. → indicating a hop from site ***i*** to ***j***, and ← the reversed hop from site ***j*** to ***i*** showcasing the asymmetry of transfer rates.

	Intra-columnar				Inter-columnar			
R_1,R_2-**D2A1**	Dimer	Sites	k_{eT} →	k_{eT} ←	Dimer	Sites	k_{eT} →	k_{eT} ←
me,tbu-	A	1 – 2	2.1×10^{13}	1.1×10^{13}	B	1 – 4	1.3×10^{12}	5.3×10^{11}
bpr,tbu-	A A‘	1 – 3 1 – 3	2.8×10^{13} 1.6×10^{12}	1.1×10^{8} 7.8×10^{6}	B	1 – 2	1.2×10^{12}	8.1×10^{11}
nbu,tbu-	A A‘	1 – 2 1 – 2	4.5×10^{12} 2.4×10^{12}	4.8×10^{6} 3.6×10^{6}	B B’ C	1 – 2 1 – 2 1 – 1	9.3×10^{10} 3.1×10^{11} 2.9×10^{11}	2.2×10^{9} 1.9×10^{9} 2.5×10^{8}
nbu,nbu-	A	1 – 2	3.9×10^{11}	4.4×10^{10}	B B’ C	1 – 3 1 – 3 1 – 4	1.5×10^{12} 1.0×10^{12} 5.2×10^{11}	8.0×10^{6} 6.4×10^{7} 8.0×10^{5}
hex,tbu-	A A‘	3 – 4 3 – 4	6.9×10^{13} 3.7×10^{13}	1.7×10^{12} 8.0×10^{11}	B	3 – 1	3.7×10^{10}	3.3×10^{10}
oct,tbu-	A A‘	1 – 2 1 – 2	9.9×10^{13} 1.5×10^{13}	3.5×10^{12} 4.8×10^{11}	B C	1 – 2 1 – 1	2.7×10^{11} 5.0×10^{10}	4.5×10^{9} 2.5×10^{10}
pyrl,tbu- **D1A1**	A	1 – 2	1.2×10^{14}	1.2×10^{11}	B	1 – 2	5.9×10^{11}	1.6×10^{8}

8. Impact of Static and Thermal Disorder onto the Mobility Tensor

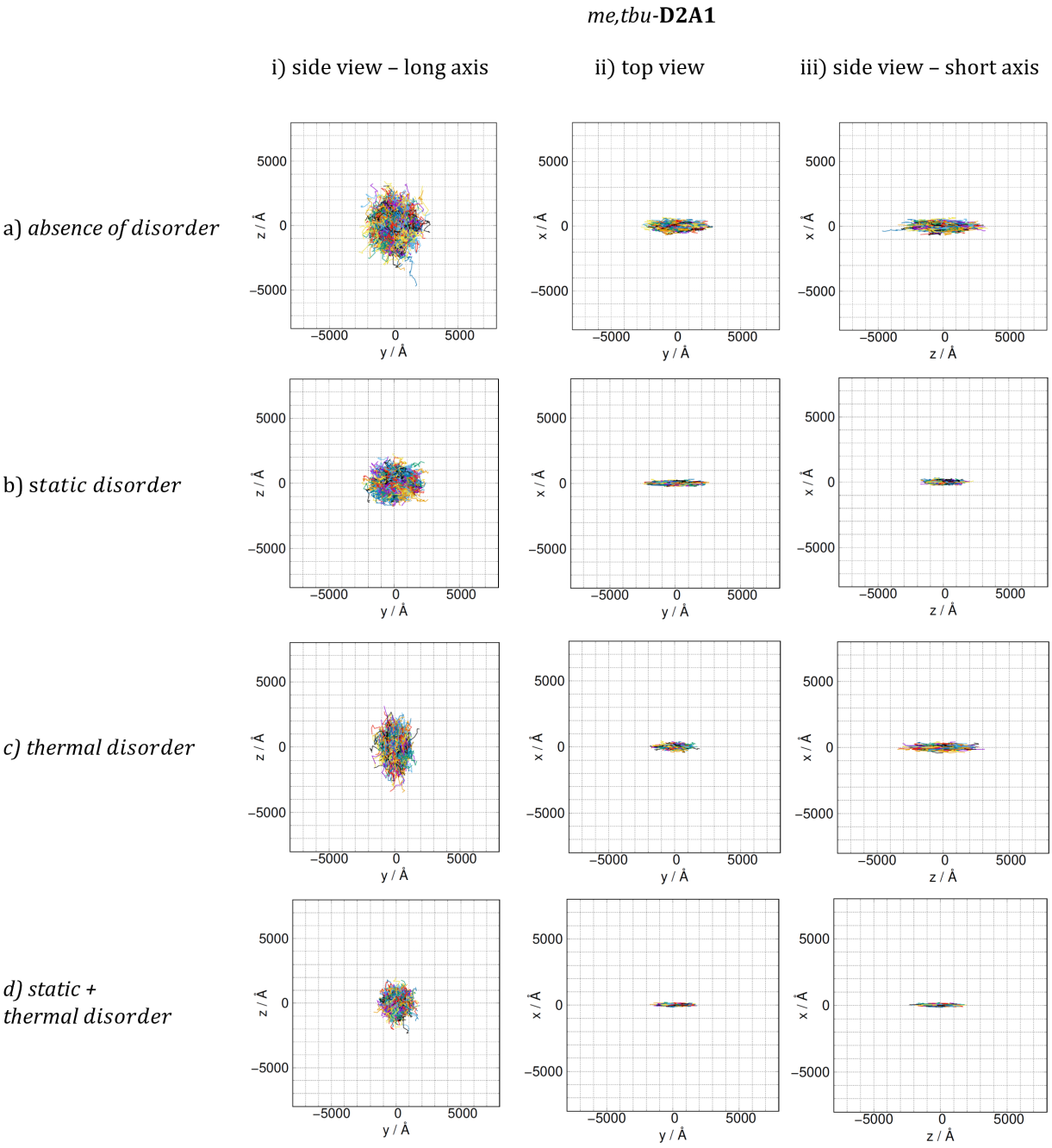

Figure S11: Plot of 1000 kMC trajectories (each consisting of 10^5 steps) for *me,tbu*-**D2A1**, a) without and b) with static disorder effects (middle panels) included, and c) when considering the thermal average of transfer integrals along the 1D column without static disorder. Trajectories are reported for the three Cartesian planes, namely xy, xz and yz. For clarity, the three Cartesian planes were ordered in such a way to correspond to i) the side view onto the molecules long axis, ii) the top view and iii) the side view onto the molecule's short axis.

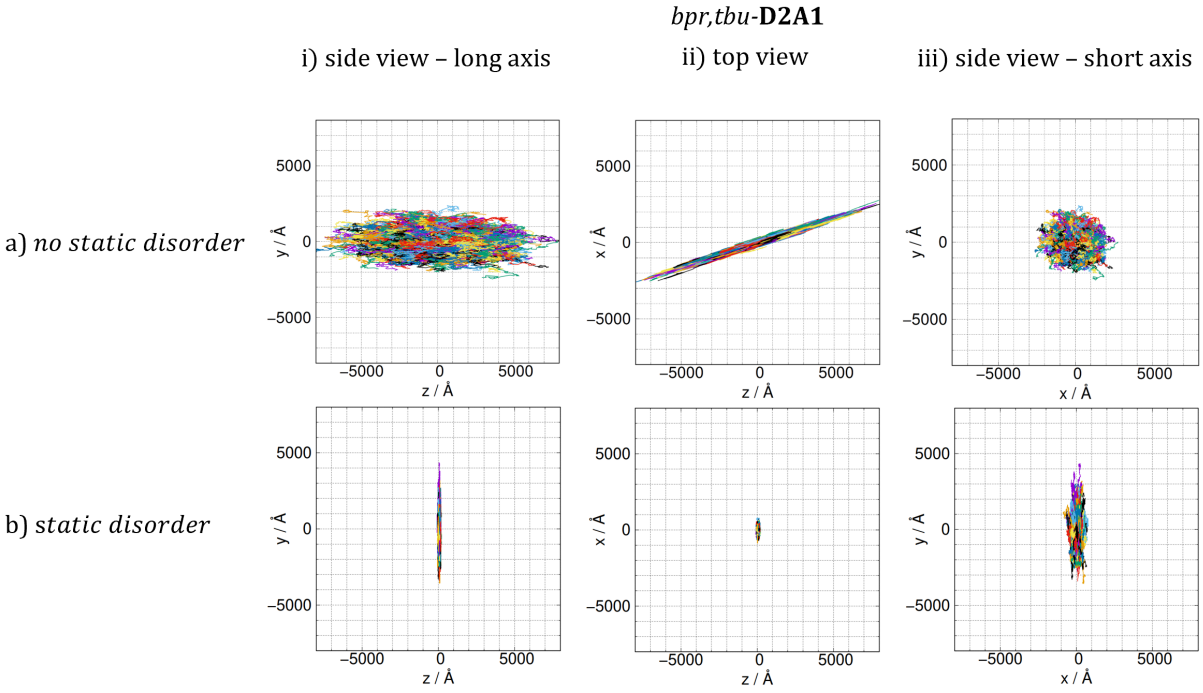

Figure S12: Plot of 1000 kMC trajectories (each consisting of 10^5 steps) for *bpr,tbu*-**D2A1**, a) without and b) with static disorder effects (lower panels) included. Trajectories are reported for the three Cartesian planes, namely xy, xz and yz. For clarity, the three Cartesian planes were ordered in such a way to correspond to i) the side view onto the molecules long axis, ii) the top view and iii) the side view onto the molecule's short axis.

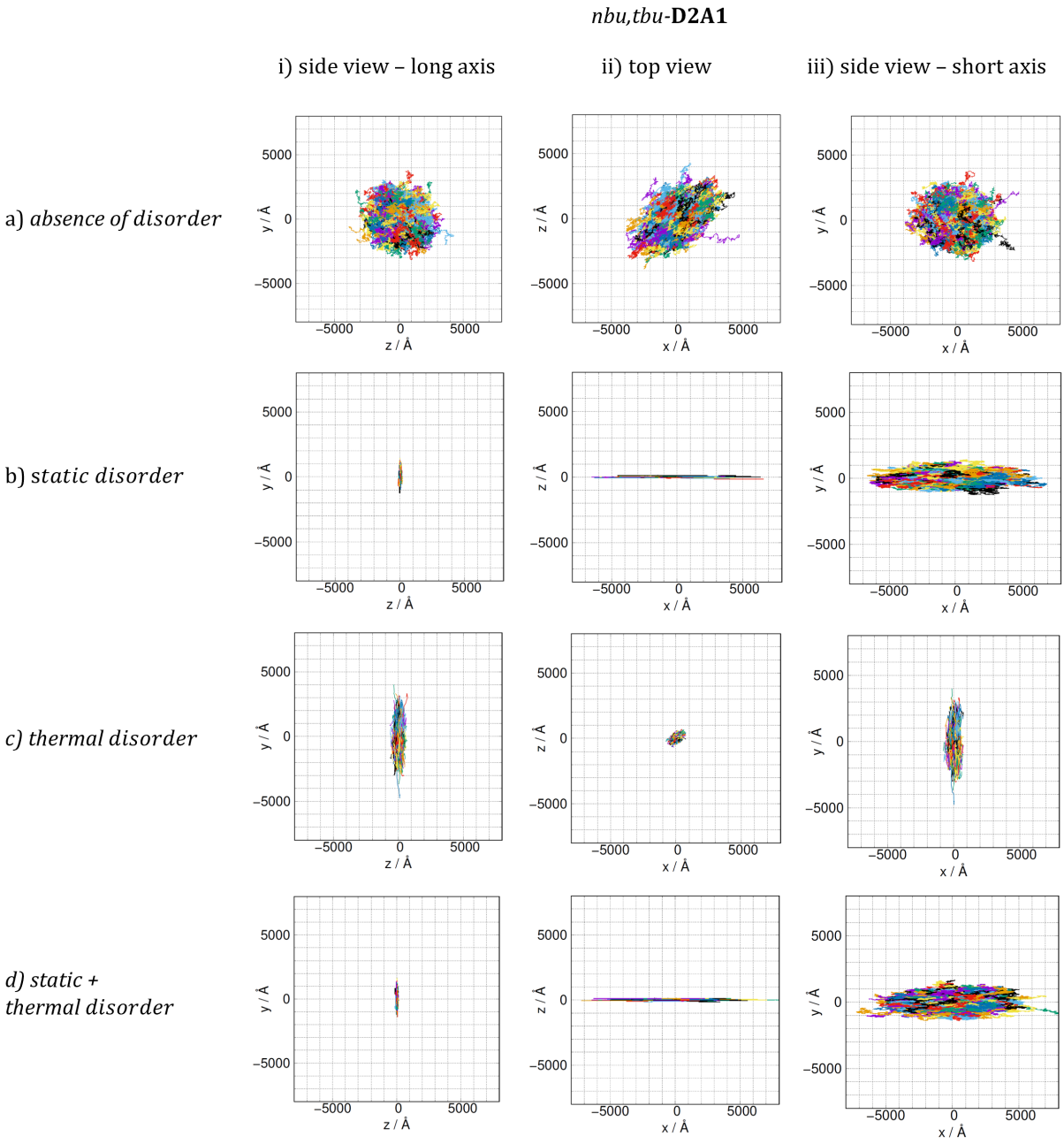

Figure S13: Plot of 1000 kMC trajectories (each consisting of 10^5 steps) for *nbu,tbu*-**D2A1**, a) without and b) with static disorder effects (middle panels) included, and c) when considering the thermal average of transfer integrals along the 1D column without static disorder. Trajectories are reported for the three Cartesian planes, namely xy, xz and yz. For clarity, the three Cartesian planes were ordered in such a way to correspond to i) the side view onto the molecules long axis, ii) the top view and iii) the side view onto the molecule's short axis.

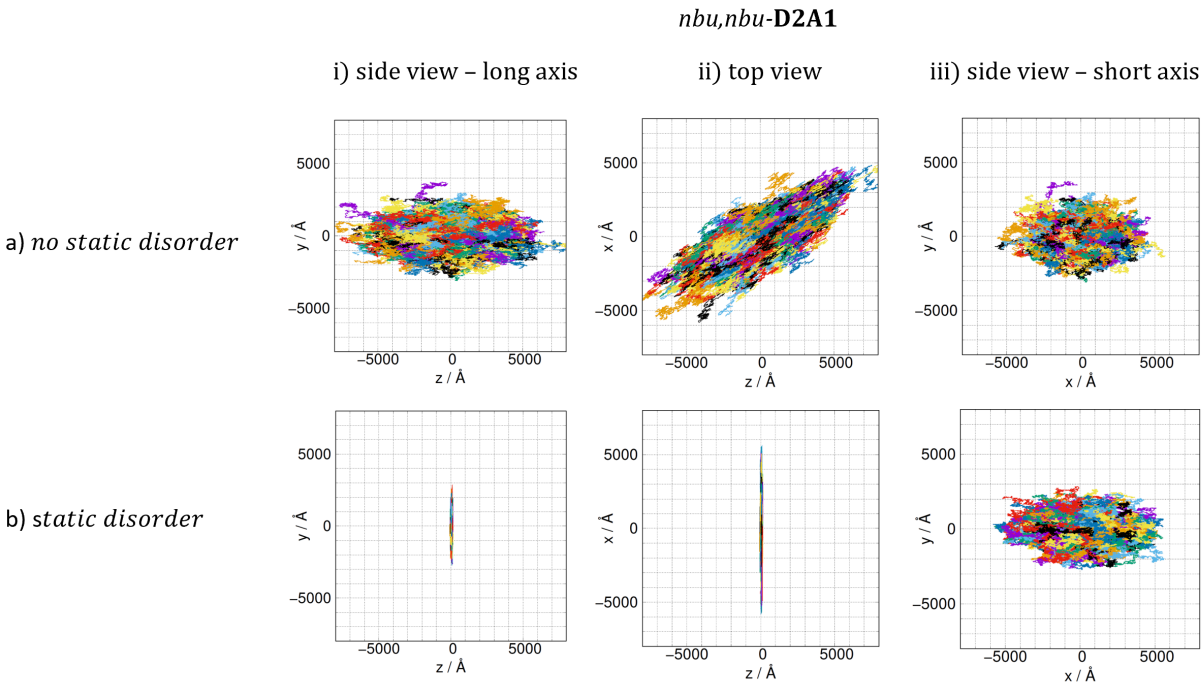

Figure S14: Plot of 1000 kMC trajectories (each consisting of 10^5 steps) for *nbu,nbu*-**D2A1**, a9 without and b) with static disorder effects (lower panels) included. Trajectories are reported for the three Cartesian planes, namely xy, xz and yz. For clarity, the three Cartesian planes were ordered in such a way to correspond to i) the side view onto the molecules long axis, ii) the top view and iii) the side view onto the molecule's short axis.

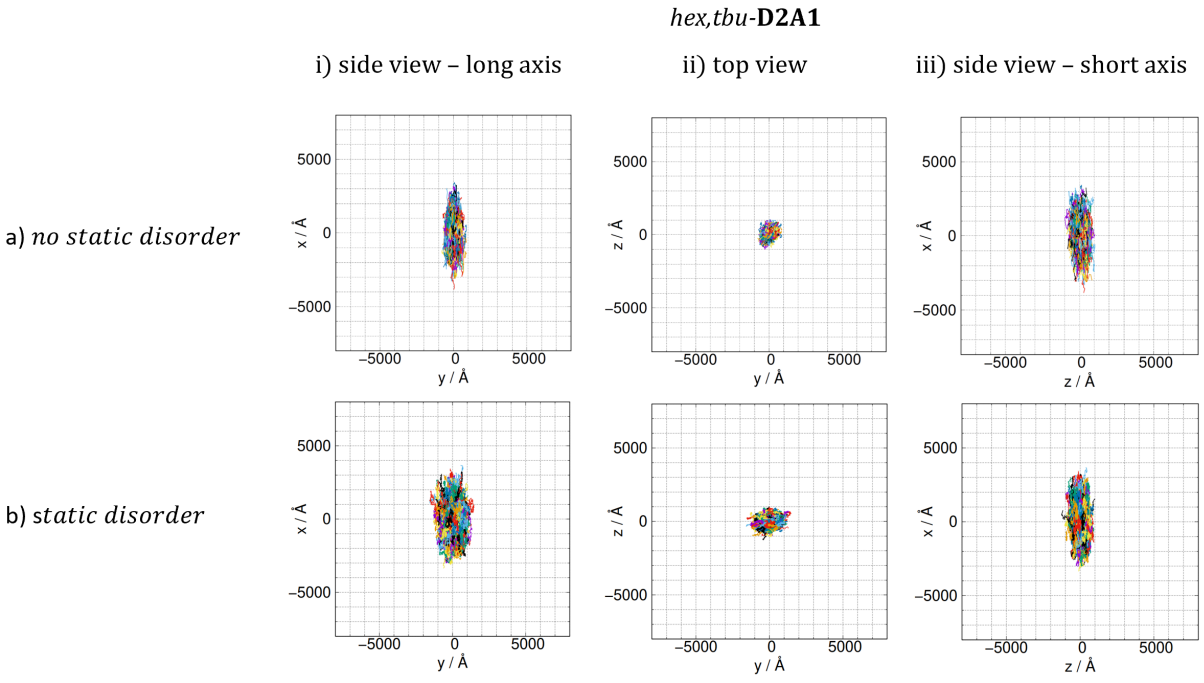

Figure S15: Plot of 1000 kMC trajectories (each consisting of 10^5 steps) for *hex,nbu*-**D2A1**, a) without and b) with static disorder effects included. Trajectories are reported for the three Cartesian planes, namely xy, xz and yz. For clarity, the three Cartesian planes were ordered in such a way to correspond to i) the side view onto the molecules long axis, ii) the top view and iii) the side view onto the molecule's short axis.

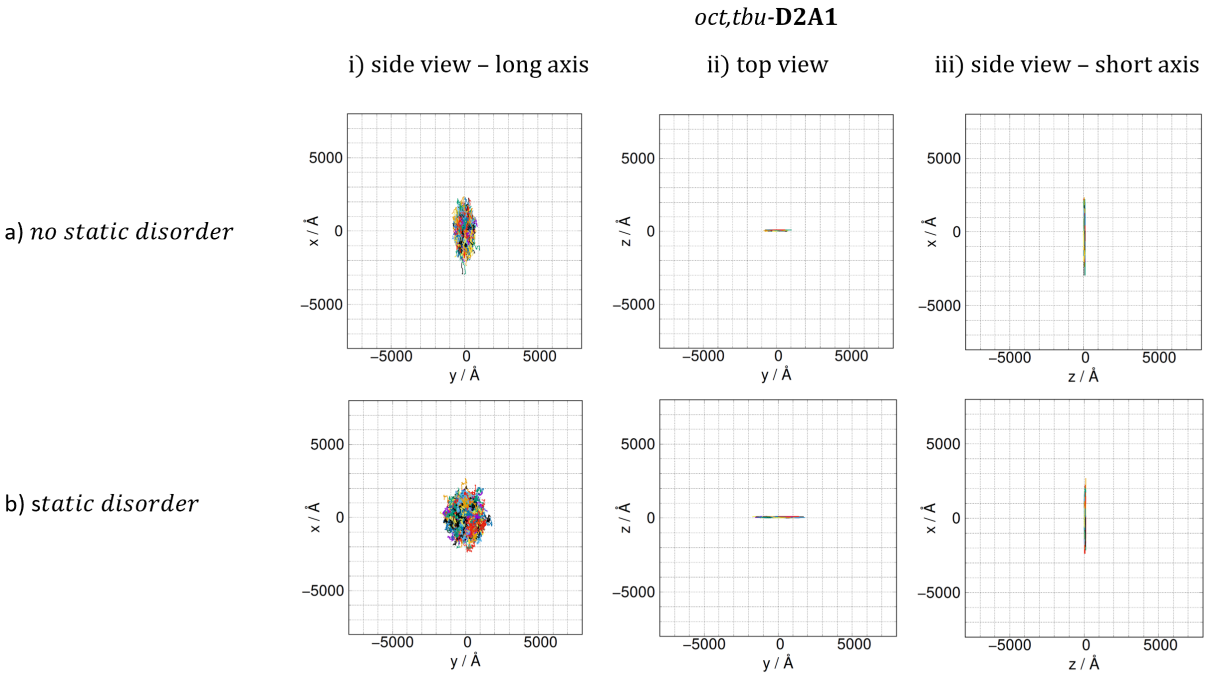

Figure S16: Plot of 1000 kMC trajectories (each consisting of 10^5 steps) for *oct,tbu*-**D2A1**, a) without and b) with static disorder effects included. Trajectories are reported for the three Cartesian planes, namely xy, xz and yz. For clarity, the three Cartesian planes were ordered in such a way to correspond to i) the side view onto the molecules long axis, ii) the top view and iii) the side view onto the molecule's short axis.

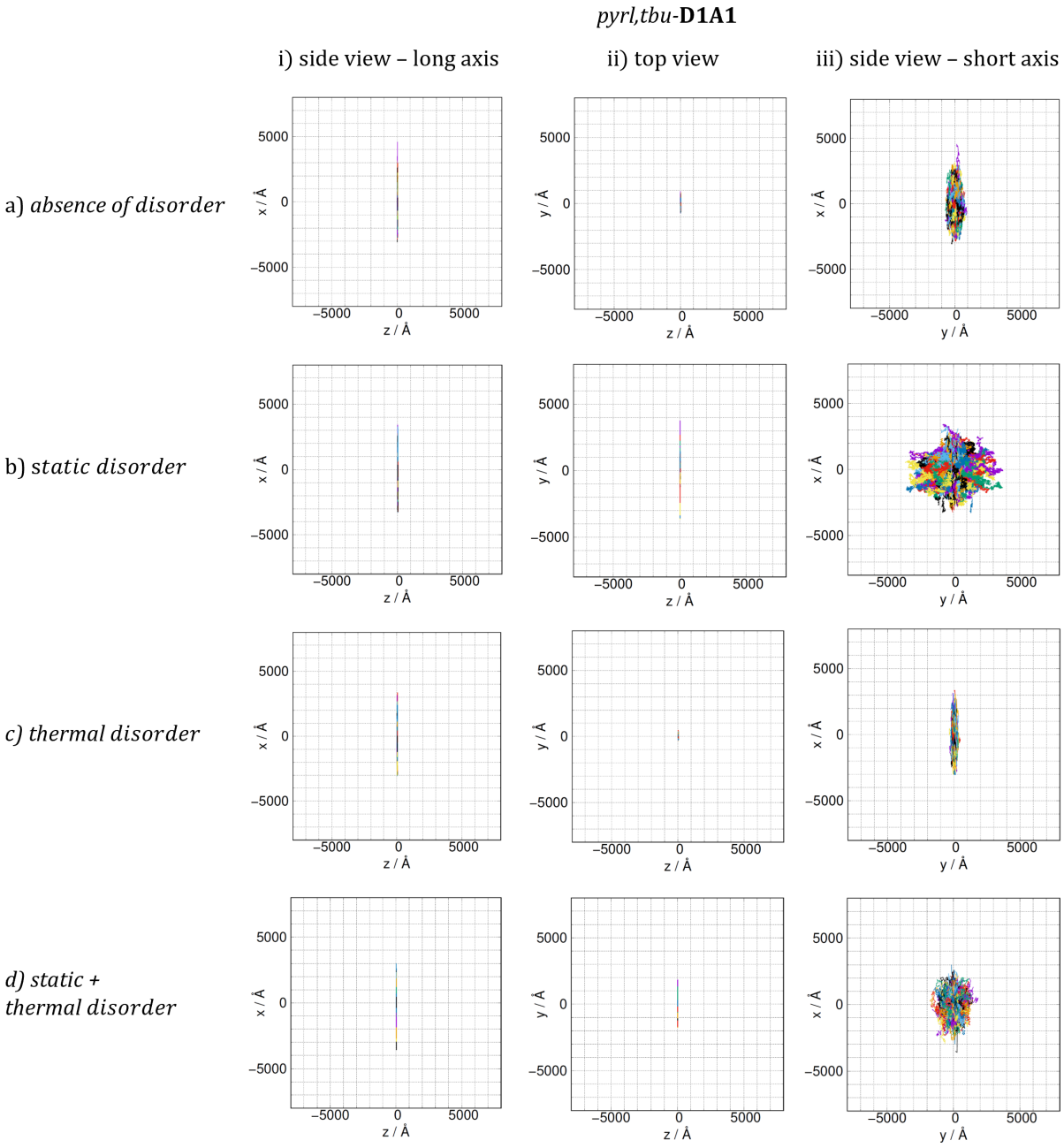

Figure S17: Plot of 1000 kMC trajectories (each consisting of 10^5 steps) for *pyrl,tbu*-**D1A1**, a) without and b) with static disorder effects (middle panels) included, and c) when considering the thermal average of transfer integrals along the 1D column without static disorder. Trajectories are reported for the three Cartesian planes, namely xy, xz and yz. For clarity, the three Cartesian planes were ordered in such a way to correspond to i) the side view onto the molecules long axis, ii) the top view and iii) the side view onto the molecule's short axis.

9. Thermal Disorder

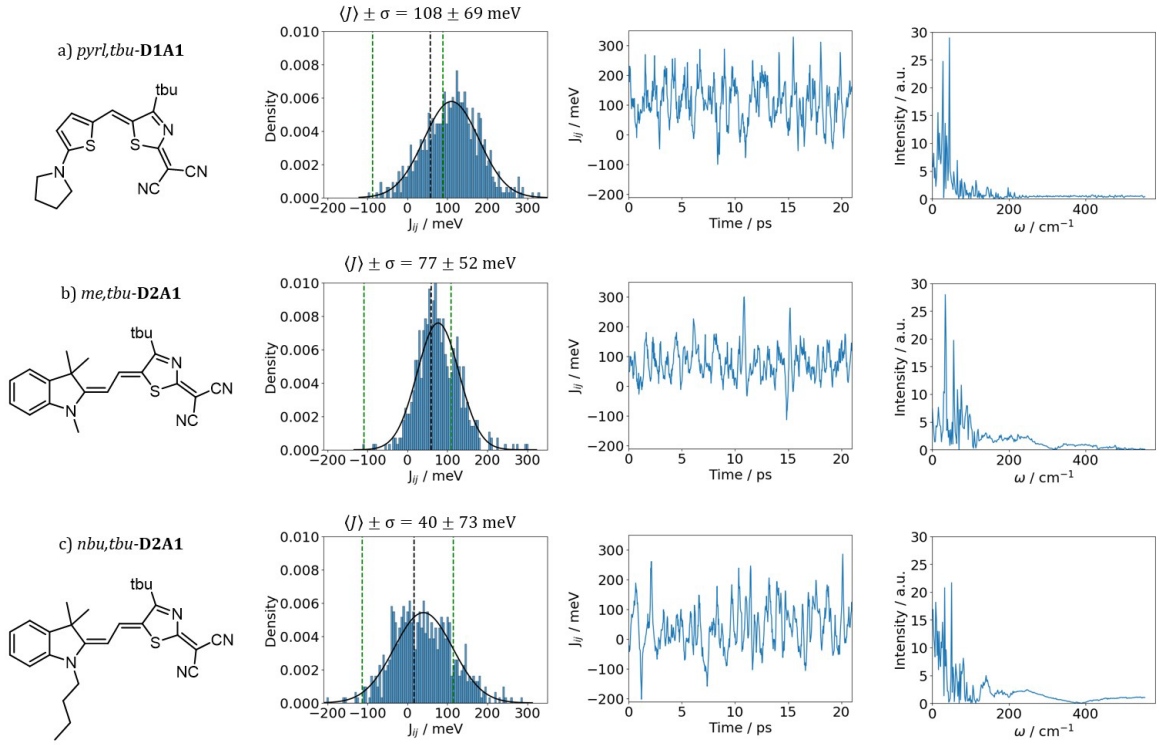

Figure S18: Dynamic disorder effects on dimer A of the crystals of a) *pyrl,tbu*-**D1A1**, b) *me,tbu*- and c) *nbu,tbu*-**D2A1**, showing the distribution of the coupling integral $\boldsymbol{J_{ij}}$ with a Gaussian git (black line), its mean value $\langle \boldsymbol{J_{ij}} \rangle$ and standard deviation $\boldsymbol{\sigma}$. Black dashed line represents the corresponding coupling in the frozen crystal and the green lines mark the $\pm\boldsymbol{\lambda/2}$ values. and fluctuations of $\boldsymbol{J_{ij}}$ over *21 ps* MD simulations, computed of snapshots every 30 fs for (middle), and the fourier transform of the autocorrelation function of the coupling integral, showing the activity of low-frequency intermolecular phonons (right).

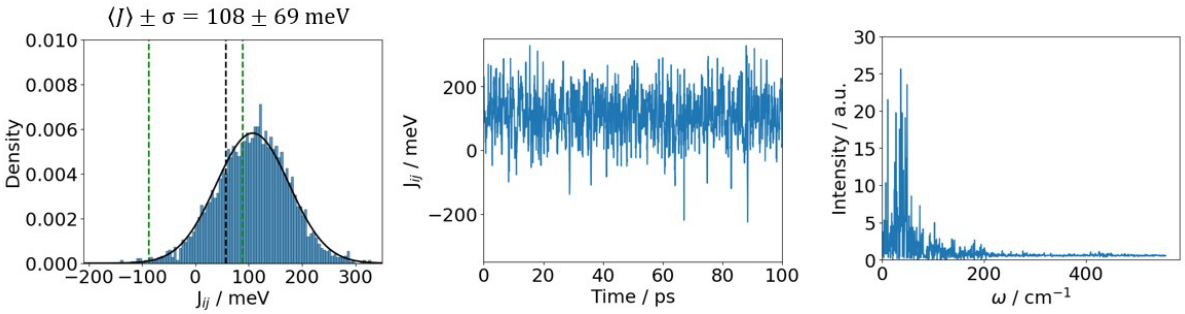

Figure S19: Dynamic disorder effects on dimer A of the crystals of *pyrl,tbu*-**D1A1** showing the distribution of the coupling integral $\boldsymbol{J_{ij}}$ with a Gaussian fit (black line), its mean value $\langle \boldsymbol{J_{ij}} \rangle$ and standard deviation $\boldsymbol{\sigma}$, as well as $\boldsymbol{\lambda/2}$ (green dotted lines) (left) and fluctuations of $\boldsymbol{J_{ij}}$ over *100 ps* MD simulations, computed of snapshots every 30 fs for (middle) and the fourier transform of the autocorrelation function of the coupling integral, showing the activity of low-frequency intermolecular phonons (right).

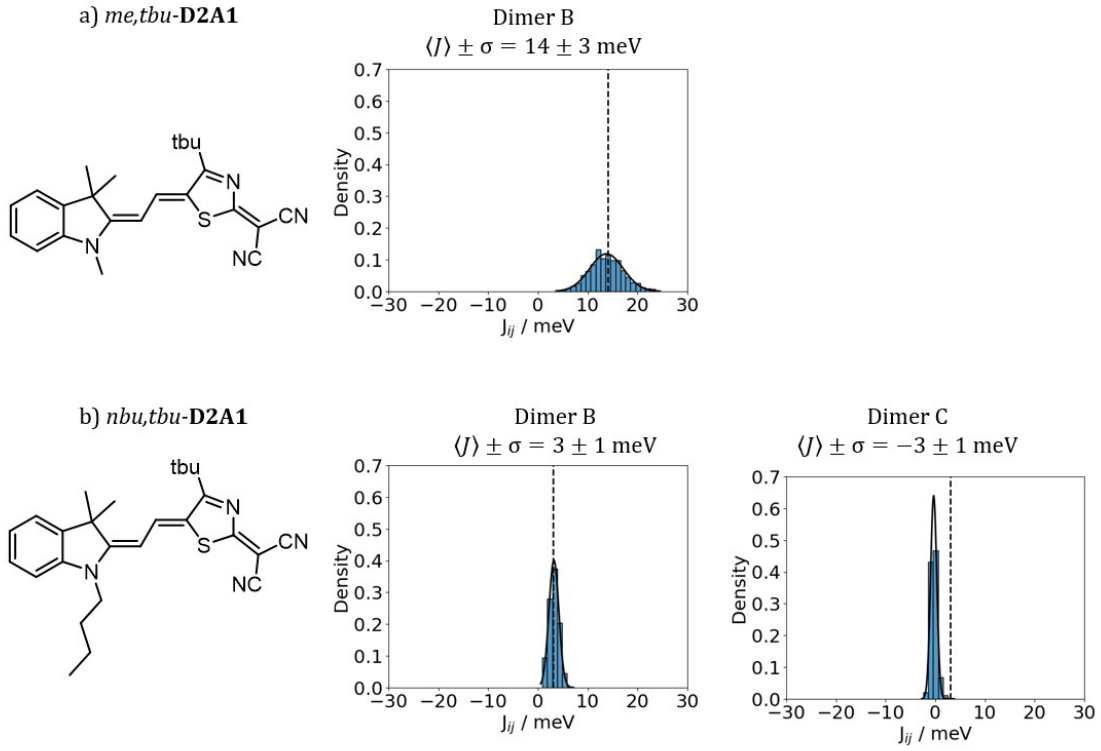

Figure S20: Dynamic disorder effects on dimer B of a) *me,tbu-* and dimer B and C of b) *nbu,tbu*-**D2A1**, showing the distribution of the coupling integral $\boldsymbol{J_{ij}}$ (Gaussian fit, black line). The mean value $\langle \boldsymbol{J} \rangle$ and standard deviation $\boldsymbol{\sigma}$ are reported as inset. Black dashed line represents the corresponding coupling in the frozen crystal.

Table S11: Coupling integrals $\boldsymbol{J_{ij}}$ from XRD structures (meV, computed with DIPRO approach at the ωB97X-D/6-311G** and Zindo/S level). Mean values $\langle \boldsymbol{J_{ij}} \rangle$ (DIPRO approach, ZINDO/S level) and standard deviation $\boldsymbol{\sigma}$ computed over 21 ps MD simulations with snapshots every 30 fs for selected dimers of *me,tbu*-**D2A1**, *nbu,tbu*-**D2A1** *pyrl,tbu*-**D1A1**. Total reorganization energy $\boldsymbol{\lambda}$ in meV, as well as adiabaticity parameter $\boldsymbol{\xi}$ and coherence parameter $\boldsymbol{\eta} = \frac{\langle J_{ij} \rangle}{\boldsymbol{\sigma}}$.

	J_{ij} (meV) ωB97X-D3/ 6-311G**	J_{ij} (meV) ZIndo/S	$\langle J_{ij} \rangle$ (meV) ZIndo/S	σ (meV)	λ (meV)	$\xi(J_{ij})$	$\xi(\langle J_{ij} \rangle)$	$\frac{\langle J_{ij} \rangle^2}{\langle {J_{ij}}^2 \rangle}$	η
me,tbu-**D2A1**	59	67	77	52	217	0.5	0.70	0.686	1.5
nbu,tbu-**D2A1**	16	7	40	73	228	0.1	0.35	0.229	0.5
pyrl,tbu-**D1A1**	56	69	108	69	177	0.6	1.22	0.716	1.6

Table S12: Average computed charge mobilities (cm²/Vs) $\boldsymbol{\mu}$ evaluated by assuming a Brownian diffusion mechanism via the Einstein-Smoluchowski equation (semi-classical Marcus equation for the transfer rates) without ($\boldsymbol{\mu_{wo}}$) and with the presence of static disorder ($\boldsymbol{\mu_s}$), thermal disorder ($\boldsymbol{\mu_t}$) or both ($\boldsymbol{\mu_{s+t}}$). Ratio between the computed charge mobility with both static and dynamic disorder with respect to the absence of disorder.

	μ_{wo} (cm²/Vs)	μ_s (cm²/Vs)	μ_t (cm²/Vs)	μ_{s+t} (cm²/Vs)	$\frac{\mu_{wo}}{\mu_{s+t}}$ (cm²/Vs)
me,tbu- ***D2A1***	0.206	0.105	0.364	0.163	0.791
nbu,tbu- ***D2A1***	0.020	0.002	0.247	0.002	0.100
*pyrl,tbu-****D1A1***	0.160	0.042	0.817	0.223	1.393

10. Thermal correction to the calculation of the non-adiabatic transfer rates

Considering the time dependent fluctuation of the transfer integral $J(t)$ in the non-adiabatic limit, the expression for the rate constant can be expressed in a series extension

$$k = k^{(0)} + k^{(1)} + k^{(2)} + \ \ldots \qquad (1)$$

where $k^{(0)}$ is the semi-classical Marcus equation

$$k^{(0)} = \frac{\langle J^2 \rangle}{\hbar} \sqrt{\frac{\pi}{\lambda k_B T}} exp\left(-\frac{(\lambda + \Delta E^0)^2}{4\lambda k_B T}\right) \qquad (2)$$

and $k^{(1)}$, $k^{(2)}$, etc. are the corrections due to the fluctuations of J. If nuclear modes are treated classically, the first non-zero correction is[2]

$$k^{(2)} = k^{(0)} 2\frac{\hbar^2}{\tau_C^2}\left[\frac{(\lambda + \Delta E^0)^2 - 2\lambda k_B T}{(4\lambda k_B T)^2}\right]\left(1 - \frac{\langle J \rangle^2}{\langle J^2 \rangle}\right) \qquad (3)$$

11. Directionality of Computed Charge Mobilities

Table S13: Computed charge mobilities hole ($\boldsymbol{\mu}$ (cm²/Vs)) evaluated by assuming a Brownian diffusion mechanism via the Einstein-Smoluchowski equation. The charge mobility is reported for the 3 cartesian directions x, y and z, as well as the average mobility overall (average_xyz) for different cases of disorder (no disorder $\boldsymbol{\mu_{wo}}$, static disorder $\boldsymbol{\mu_s}$ and thermal disorder $\boldsymbol{\mu_t}$).

		$\boldsymbol{\mu}$ (cm²/Vs)		
		no disorder μ_{wo}	static disorder μ_s	thermal disorder average μ_t
R_1,R_2-**D2A1**	direction			
me,tbu-	average_xyz	0.206	0.105	0.364
	x	0.013	0.003	0.014
	y	0.243	0.203	0.257
	z	0.370	0.119	0.791
bpr,tbu-	average_xyz	0.161	0.007	-
	x	0.044	0.001	-
	y	0.034	0.020	-
	z	0.403	0.000	-
nbu,tbu-	average_xyz	0.020	0.002	0.247
	x	0.025	0.005	0.032
	y	0.016	0.000	0.699
	z	0.019	0.000	0.024
nbu,nbu-	average_xyz	0.030	0.004	-
	x	0.026	0.010	-
	y	0.009	0.002	-
	z	0.059	0.000	-
hex,tbu-	average_xyz	0.067	0.018	-
	x	0.169	0.044	-
	y	0.012	0.007	-
	z	0.017	0.004	-
oct,tbu-	average_xyz	0.065	0.017	-
	x	0.166	0.034	-
	y	0.027	0.016	-
	z	0.003	0.001	-
pyrl,tbu- **D1A1**	average_xyz	0.160	0.042	0.817
	x	0.453	0.117	2.468
	y	0.028	0.010	0.041
	z	0.001	0.001	0.005

12. References

1 N. Gildemeister, G. Ricci, L. Böhner, J. M. Neudörfl, D. Hertel, F. Würthner, F. Negri, K. Meerholz and D. Fazzi, *J. Mater. Chem. C*, 2021, **9**, 10851–10864.

2 A. Troisi, *Molecular Simulation*, 2006, **32**, 707–716.